

## CT-based assessment of regional pulmonary microvascular blood flow parameters

Chulho Won, Deokiee Chon, Jehangir Tajik, Binh Q. Tran, G. Blake Robinswood, Kenneth C. Beck, and Eric A. Hoffman

Departments of Radiology and Biomedical Engineering, University of Iowa, Iowa City, Iowa 52241

Submitted 26 July 2002; accepted in final form 23 January 2003

**Won, Chulho, Deokiee Chon, Jehangir Tajik, Binh Q. Tran, G. Blake Robinswood, Kenneth C. Beck, and Eric A. Hoffman.** CT-based assessment of regional pulmonary microvascular blood flow parameters. *J Appl Physiol* 94: 2483–2493, 2003. First published February 14, 2003; 10.1152/jappphysiol.00688.2002.—To determine regional pulmonary microvascular mean transit times (MTTs), we used electrocardiogram-gated X-ray computed tomographic imaging to follow bolus radiopaque contrast material through the lungs in anesthetized animals (7 dogs and 1 pig, prone and supine). By deconvolution/reconvolution of regional time-attenuation curves obtained from parenchyma and large lobar arteries, we estimated the microvascular residue function and reconstituted the regional microvascular time-attenuation curves and, thus, regional microvascular MTTs. The mean microvascular MTTs in the supine and prone postures were  $3.94 \pm 1.0$  and  $3.40 \pm 0.84$  (mean  $\pm$  SD), respectively. The dependent-nondependent vertical gradient of MTT was greater in the supine [slope =  $0.25 \pm 0.10$  (SD),  $P < 0.001$  by *t*-test] than in the prone ( $-0.03 \pm 0.06$  in 6 of 8 animals; 2 outliers had positive slopes) posture. In both postures, there was a trend toward faster transit times in the dorsal-basal lung region in six of the eight animals, suggesting gravity-independent higher vascular conductance dorso-caudally. We conclude that deconvolution methods, in association with electrocardiogram-gated high-speed X-ray computed tomography, can provide insights into regional heterogeneity of pulmonary microvascular MTT in vivo.

capillary mean transit times; pulmonary blood flow; pulmonary imaging; computed tomography; regional perfusion; physiological imaging; electron beam computed tomography; multidetector computed tomography; lung; pulmonary physiology; deconvolution; quantitative computed tomography

DYNAMIC MULTISLICE X-ray computed tomographic (CT) imaging of the pulmonary system, when combined with a suitable radiopaque tracer agent, offers the ability to measure, in vivo and in detail, regional pulmonary perfusion throughout the lungs (13, 14, 16, 25, 26). Of particular interest in pulmonary physiology are measurements of the time red blood cells (RBCs) spend at the alveolar-capillary interface and, thus, the amount of time available for gas exchange (31). Several approaches have been used to measure the capillary transit times either directly or indirectly (6): diffusing capacity at multiple O<sub>2</sub> concentrations, allowing calcu-

lation of global capillary blood volume and mean transit time (MTT); in vivo microscopy, allowing measurement of RBC transit times in vessels at the lung surface (32); and magnetic resonance imaging using tracer gases (10). Electron beam CT (EBCT) allows fast (50–100 ms) acquisition of data necessary for cardiac gated imaging of passage of a radiopaque dye to obtain regional perfusion. EBCT, as well as other forms of X-ray CT scanning, has been used in animal and clinical studies of perfusion and ventilation (16, 19, 25, 27).

Given their resolution limits, whole body CT scanners are not able to resolve individual capillary beds, and regions of interest (ROIs) placed in the lung field of a dynamic image sequence most certainly contain contaminating flow signals from small arteries and veins in addition to the microvascular bed. Because we are often interested in the microvascular flow and transport characteristics, we have developed a method to extract the microvascular flow signal from regional parenchymal time-attenuation curves.

In this study, our aim was to evaluate a noninvasive CT-based method for characterizing the distribution of microvascular MTT and to use this method to evaluate microvascular MTT in animals (dogs and a pig) in the supine and prone body postures. In addition, we use a Monte Carlo simulation to estimate error in the derived microvascular perfusion parameters.

### METHODS

**EBCT.** Scanning protocols utilize an EBCT scanner (model C-150L, Imatron, South San Francisco, CA) (4). This scanner differs from conventional X-ray CT scanners, in that a focused electron beam is swept along tungsten targets surrounding the animal, instead of mechanical rotation of an X-ray source around the animal. This design allows for fast tomographic image acquisition, with scan apertures on the order of 50–100 ms, as opposed to ~0.6- to 1.0-s scan apertures from other high-speed commercial X-ray CT scanners. The fast scan times available with EBCT allow us to obtain stop-action images of the heart and allow us to minimize lung density changes induced by the effect of cardiac motion.

The EBCT scanner operates in a high temporal resolution mode (multi-time-point imaging) or in a high spatial resolution mode (volumetric imaging). In the high temporal resolution mode, the electron beam is magnetically steered se-

Address for reprint requests and other correspondence: E. A. Hoffman, Dept. of Radiology, University of Iowa College of Medicine, 200 Hawkins Dr., Iowa City, IA 52242 (E-mail: eric-hoffman@uiowa.edu).

The costs of publication of this article were defrayed in part by the payment of page charges. The article must therefore be hereby marked “advertisement” in accordance with 18 U.S.C. Section 1734 solely to indicate this fact.

quentially along four tungsten target rings encompassing 210° about the animal. X-rays produced from each target ring are focused onto two detector rings, so that up to eight spatial levels may be acquired at each time point. Each pair of images is gathered within 54 ms followed by an 8-ms pause as the beam is reset for the next target ring. All eight spatial levels are therefore acquired within 224 ms. The axial resolution for the multi-time-point imaging mode is 1.5–3.0 mm if only a single tomographic slice is to be acquired over multiple time points or 7 mm if the multislice mode (up to 8 spatial tomographic levels covering 7 cm) is used in conjunction with multi-time-point imaging.

**Animal preparation.** All animal studies were performed within guidelines for animal care adhered to by the American Physiological Society and the National Institutes of Health. The animals were studied at the University of Pennsylvania or the University of Iowa, with approval from the respective institutional Animal Care and Use Committees.

Seven dogs (12–25 kg, 4 beagles and 3 mongrels) were anesthetized with fentanyl and pentobarbital sodium (25 mg/kg). The pig was premedicated intramuscularly with ketamine (1 mg/kg) and acepromazine, and anesthesia was induced with a bolus (2.5 mg/kg) of propofol (Diprivan) in an ear vein. Anesthesia was maintained via halothane until a cuffed endotracheal tube was placed via tracheostomy. Deep anesthesia was maintained with continuous propofol (12 mg·kg<sup>-1</sup>·h<sup>-1</sup> iv) drip titrated to heart rate and reflexes.

After the endotracheal tube was placed and inflated, all animals were mechanically ventilated (10 ml/kg, 12–15 breaths/min) with a Harvard piston pump respirator. Pressure catheters (liquid-filled or Millar) were inserted into peripheral major arteries (carotid and femoral) and veins (jugular and femoral) via a cut-down procedure. Under fluoroscopic guidance, catheters were advanced to the right ventricle, right main pulmonary artery, and left ventricle for measurement and recording of physiological information.

After catheterization, animals were transported to the EBCT scanner facility at the respective institution, placed supine on the scanner table, and connected to and ventilated by a computer-controlled respirator (model CTP9000, CWE, Ardmore, PA). Electrocardiogram, airway pressure, left and right ventricular pressures, and pulmonary arterial pressure were monitored using an IBM-compatible computer equipped with a standard laboratory analog-to-digital converter board and recording software. The scanner “X-ray on” pulse was also recorded to allow exact correlation of physiological and scanner events. Throughout the catheterization procedures and scanning protocols, deep anesthesia was maintained with continuous drip (12 mg·kg<sup>-1</sup>·h<sup>-1</sup> iv) of propofol titrated to heart rate and reflexes. At the conclusion of scanning, each animal was euthanized with pentobarbital sodium (60 mg/kg) and concentrated KCl.

**Perfusion imaging protocol.** Regional perfusion measurements were made using dynamic EBCT to follow bolus radiopaque contrast passage through the lung field. The EBCT scanner was used in the high temporal resolution (flow) mode, acquiring 6 or 8 spatial levels at 10–13 time points each. The topmost tomographic slice was centered about the carina. All animals were imaged in supine and prone postures during a brief period of apnea (10–12 s) with the lungs held at 0 cmH<sub>2</sub>O airway pressure (functional residual capacity) during imaging gated to 80% of the R-R interval of the electrocardiogram complex. Nonionic radiopaque contrast agent (0.5–1.0 ml/kg; Omnipaque 240 or 350) was injected over 2–3 s via a powered injector connected to a 7F multiple-side-hole catheter placed in the right ventricular outflow tract. Contrast agent was injected at least one heartbeat

after scan initiation to ensure at least one baseline point before contrast arrival.

The acquired time-attenuation data were fit to gamma variate functions (8, 29), and, on the basis of our preliminary results, the gamma variate functions were resampled with a temporal resolution of 0.1 s.

**Perfusion image analysis.** Specific ROIs in the images were sampled in two ways for analysis: 1) specific ROIs were manually chosen to include parts of larger arteries to demonstrate the partial volume effects of including larger vessels with parenchymal regions, and 2) areas of lung parenchyma were sampled automatically by the computer using an ROI of 12.5–20.0 mm, with 7- to 8-mm slice thickness. We were careful to collect data representing only the parenchymal regions within a lung field. Samples with partial volume problems associated with regions close to the mediastinal or chest wall borders (rib cage and diaphragm) and myocardium were eliminated. Several additional criteria were established to eliminate regions containing major pulmonary blood vessels (veins and arteries) and major airways. Our laboratory previously demonstrated that, at functional residual capacity, normal lung density of a supine or prone dog ranges from ~35 to 90% air content (12). To ensure that we accepted no ROIs through which major airways or major vessels traversed, we eliminated all samples with baseline lung density >90% or <40%. Also, regions that could not be fit using the algorithms described below were discarded. After the elimination process, depending on the quality of the data set, there were 500–1,500 samples per right or left lung. This process resulted in a grid of voxels, each with a value for MTT, regional air content, and position coordinates. These regions were used to analyze the distribution of MTT within the lung using univariate regression or multiple linear regression.

Perfusion image data were analyzed according to a bolus injection, residue detection model (2). In this model, the bolus is assumed to travel essentially unmodified from the site of injection (right ventricular outflow tract) through the pulmonary arterial system. The bolus then enters the microvascular bed and is dispersed according to the distribution of particle transit times through the microvascular bed. The time-attenuation signal measured in the lung parenchyma is thus due to the interaction of bolus delivery and the fraction of the bolus residing in the regional microvascular bed (residue or retention function) at any given time. The interaction of two functions or processes (bolus delivery and bolus retention in the microvascular bed) is described by the mathematical process of convolution of the feeding pulmonary artery input [ $X_{PA}(t)$ ] and the regional residue function [ $R(t)$ ], resulting in the measured regional parenchymal time-attenuation curve [ $Y_{ROI}(t)$ ]. This relation is represented as follows

$$Y_{ROI}(t) = X_{PA}(t) \otimes R(t) \quad (1)$$

where  $\otimes$  denotes the convolution operator.

Figure 1 shows the locations of input and output data, where the input ROI is selected in the center of the feeding pulmonary artery and the output data are chosen from the regional microvascular bed. A nonlinear model of the Marquardt method is used to fit a gamma variate function to the concentration-time course. To avoid effects of recirculation, we excluded all points with a value less than that which represented 50% of the magnitude between the baseline and the peak. Fitted input and output curves are shown in Fig. 1B. Deconvolution of the measured pulmonary artery and regional parenchymal time-attenuation curves thus provides a method for obtaining the regional residue function (fraction of bolus residing, or remaining, in the local microvascular bed

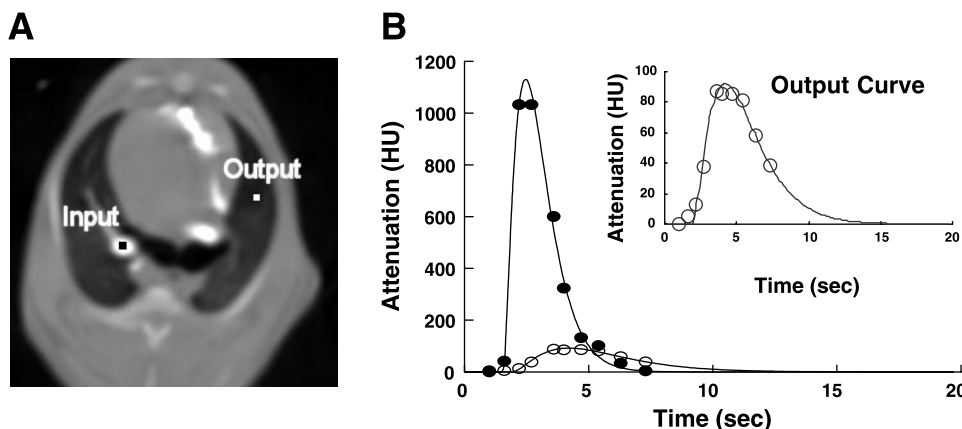


Fig. 1. Sample locations of feeding pulmonary artery (input) and parenchymal (output) regions of interest on transverse plane in supine position (A) and gamma variate-fitted input and output curves corresponding to locations (B). Size of region of interest (ROI) consists of  $5 \times 5$  pixels, where a pixel was 0.08 mm on a side. HU, Hounsfield units.

at any given time). The MTT of the residue function (hence, local microvascular bed) can then be calculated as follows (1)

$$MTT = \frac{\int R(t)dt}{R_{max}} \quad (2)$$

where  $R_{max}$  is the peak of the regional residue function.

*Deconvolution method.* We implemented two deconvolution methods [the fast Fourier transformation (FFT) and the damped least squares (DLS) methods] to verify, through cross validation, our result of deconvolution of the measured pulmonary artery and regional parenchymal time-attenuation curves. Before the two methods were applied, the input (feeding pulmonary artery) curve data were made to be the same length as the regional parenchymal (output) curve by addition of zeroes at the end. The sampled gamma variate functions were then deconvolved.

Using the FFT, convolution in the time domain of Eq. 1 is represented simply by an algebraic relation in the frequency domain. Thus Eq. 1 can be rewritten as follows

$$Y_{ROI}(\omega) = F\{X_{PA}(t)\} * F\{R(t)\} = X_{PA}(\omega) * R(\omega) \quad (3)$$

where  $\omega$  indicates angular frequency.

To obtain the regional residue function  $[R(\omega)]$  deconvolution, implemented in the frequency domain, is the quotient of the transform of the measured regional time-attenuation curve  $[Y_{ROI}(\omega)]$  and the feeding pulmonary artery function  $[X_{PA}(\omega)]$ . The time domain regional residue function can be obtained by applying the inverse FFT

$$R(t) = F^{-1}\{R(\omega)\} = F^{-1}\left\{\frac{Y_{ROI}(\omega)}{X_{PA}(\omega)}\right\} \quad (4)$$

where  $F\{\}$  and  $F^{-1}\{\}$  denote the Fourier transform and the inverse Fourier transform, respectively (20).  $R(t)$  can be determined by taking the inverse FFT of the ratios of the transforms of the arterial input and parenchymal output curve, as shown in Eq. 4. We have found that deconvolution of the feeding pulmonary artery and regional parenchymal time-attenuation curves resulted in bimodal residue functions consisting of an overlapping sharp, narrow peak and a second, more dispersed peak (Fig. 2). To show the correctness of a bimodal nature of the residue function, we applied an algebraic DLS approach, which is the algorithm that simultaneously constructs a least squares solution to the discrete form of Eq. 5 while damping the oscillations inherently present in the algebraic solution (7, 22)

$$R_{ROI}(t_j) = \int_0^t X_{PA}(t-s)R(s)ds \approx \Delta t \sum_{i=0}^j X_{PA}(t_j-t_i)R(t_i) \quad (5)$$

Figure 2 shows that the DLS method produces the same residue function, which contains an overlapping sharp, narrow peak and a second, more dispersed peak similar to the FFT method. Reconvolving with the feeding pulmonary artery (input) yields the same curve as the original parenchymal time-attenuation curve (output), yielding one further piece of evidence that our deconvolution was correctly performed (Fig. 3).

*Separation of the residue function and calculation of contamination.* The sharp, narrow peak in the residue function is likely due to partial volume sampling of small arteries with microvascular content. Regional residue functions of samples containing a visually apparent arterial vessel exhibit virtually only the unimodal prominent sharp, narrow peak. After the regional arterial and microvascular curves had been separated from the bimodal residue function (28), we observed a decrease in the peak amplitude of the arterial residue curve from dependent to nondependent lung regions in supine, but not prone, animals (Fig. 4). In the supine posture, this is consistent with known physiology, wherein fewer arterial regions are expected in the nondependent lung, since the lung is less dense and more fully inflated, whereas lung inflation is more uniform in the prone posture.

By separating the bimodal residue functions obtained using deconvolution techniques into residue functions for the arterial  $[R_{art}(t)]$  and microvascular  $[R_{mic}(t)]$  components, we

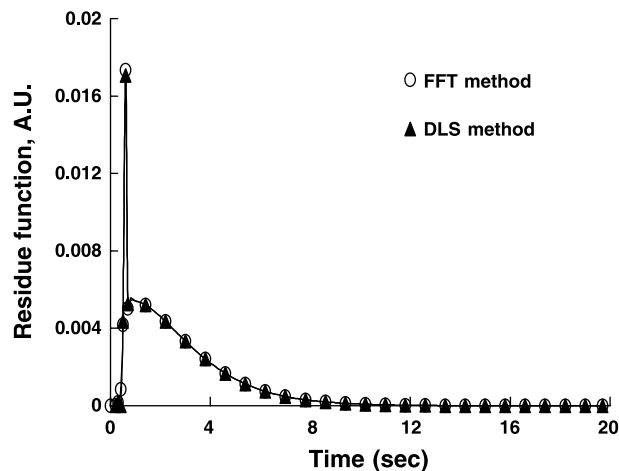


Fig. 2. Residue functions obtained by using fast Fourier transform (FFT) and damped least squares (DLS) deconvolution methods. The 2 residue functions are almost identical. Both residue functions have a bimodal nature that consists of a first sharp, narrow peak and a second more dispersed peak. AU, arbitrary units.

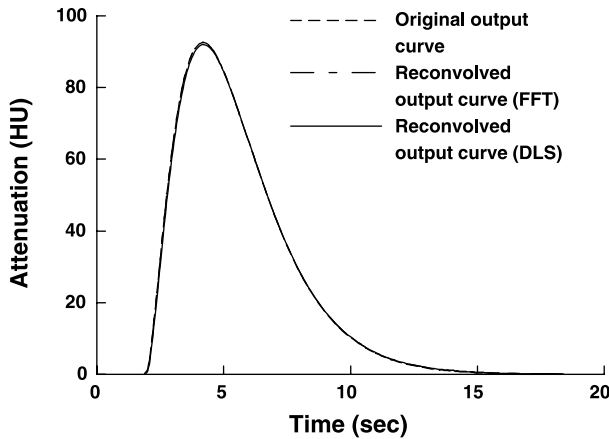


Fig. 3. Fitted original output curve and 2 output curves obtained by reconvolving the 2 residue functions in Fig. 2 with the feeding arterial curve (input). The 3 curves are essentially indistinguishable from one another, lending strength to the notion that the 2 residue functions produced by the FFT and DLS deconvolution methods are correct.

were able to compute the proportion of the regional time-intensity curves associated with each. This is done by reconvolving with the feeding pulmonary artery input function with the respective residue functions to produce  $Y_{art}(t)$  and  $Y_{mic}(t)$ , respectively. Regional arterial signal contamination was then calculated by comparing the areas of the arterial time-attenuation curve with the original parenchymal curve. Alternatively, arterial contamination can be obtained by ex-

amining the ratios of the adjusted microvascular and original parenchymal curves

$$\text{Arterial contamination (\%)} = \frac{\int Y_{art}(t)dt}{\int Y_{ROI}(t)dt} = 1.0 - \frac{\int Y_{mic}(t)dt}{\int Y_{ROI}(t)dt} \quad (6)$$

*Monte Carlo simulations.* Random errors were superimposed on the known, measured input (pulmonary artery) and output (regional parenchymal) time-attenuation curves obtained as described above. The resulting simulated data were fit to gamma variate functions and processed via the deconvolution algorithm described above to provide microvascular MTTs for the simulated curves. The error superimposed on the known input and output signals was obtained by assessing EBCT-derived CT images using two different noise content measurement methods (see APPENDIX).

Each simulation consists of the following four steps: 1) the feeding and regional parenchymal time-attenuation curves were chosen from dog images and fitted by a gamma variate function; 2) each of two noise measures (global and local noises) were added to the corresponding attenuation value at each time point of the fitted pulmonary artery and parenchymal time-attenuation curves, respectively, obtained above; 3) data that were modified by addition of noise were fitted, deconvolved, and isolated, as described above; 4) a MTT for the microvascular bed was calculated as the ratio of area to peak of the microvascular component of the residue function (see APPENDIX).

*Statistical analysis.* Microvascular MTTs were evaluated with respect to height from the basal regions of the lungs in the supine and prone positions. Basal regions were chosen for imaging, because this is where the greatest vertical height of

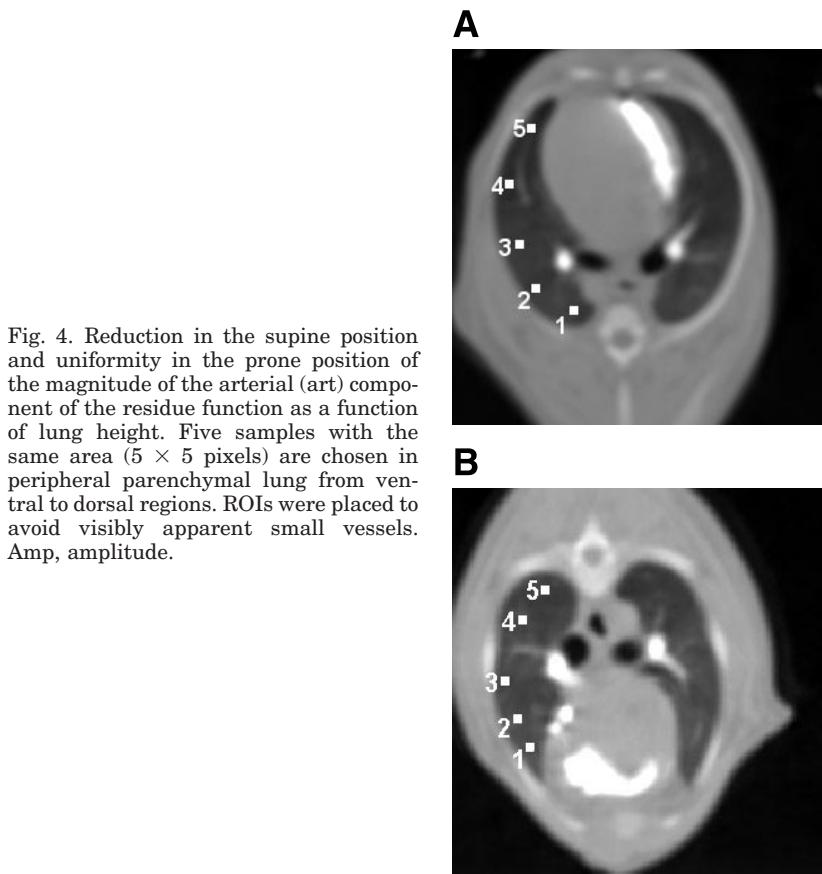
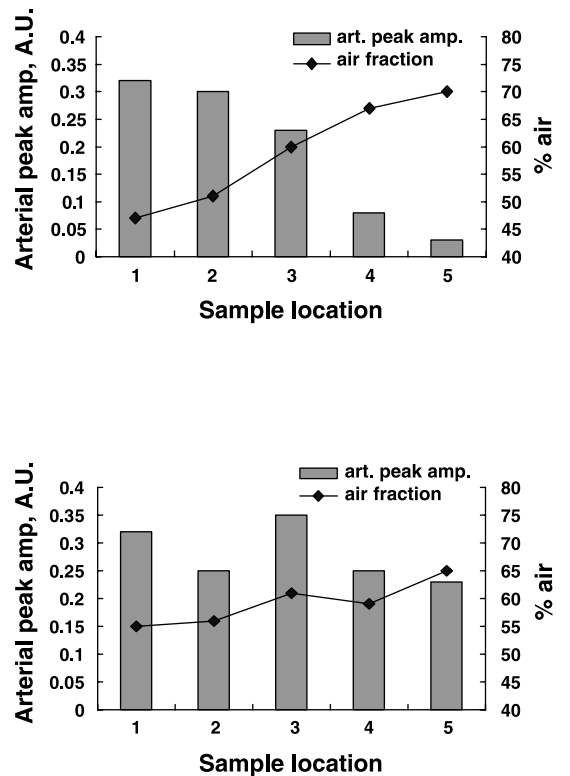


Fig. 4. Reduction in the supine position and uniformity in the prone position of the magnitude of the arterial (art) component of the residue function as a function of lung height. Five samples with the same area ( $5 \times 5$  pixels) are chosen in peripheral parenchymal lung from ventral to dorsal regions. ROIs were placed to avoid visibly apparent small vessels. Amp, amplitude.



lung could be found. Each animal was scanned once in each position, producing six to eight sagittal images. Microvascular MTTs were computed in a grid of ROIs, as described above, in each slice. The vertical gradient in MTT was obtained using univariate linear regression and model-independent averaging, obtained by calculating the mean MTT for dependent and nondependent regions of the lungs. The dependent region is defined as the area 5–30% of the height from the base of the lung, and the nondependent region is defined as the area 70–95% of the height from the base of the lung.

## RESULTS

To demonstrate the effect of partial-volume arteries on the first sharp peak of the residue function, we selected ROIs in which we purposely included more or less of the edge of a large pulmonary artery along with parenchyma (Fig. 5A) and ROIs that included clearly visible small arteries (Fig. 5B). Figure 5 shows the positive relation between the amount of arterial com-

ponent in the ROI and the magnitude of the sharp, narrow arterial peak in the associated residue function. This can be represented by a contamination index shown in Eq. 6. In Fig. 5A, inasmuch as the ROI contains a greater portion of the feeding pulmonary artery, arterial contamination increases from 6.4 to 18.9%. Also, in Fig. 5B, inasmuch as peripheral ROIs include larger visibly apparent pulmonary vessels, the contamination index is seen to increase (from 8.5 to 18.5%).

The mean microvascular MTTs in the supine and prone postures were  $3.94 \pm 1.03$  and  $3.40 \pm 0.84$  (SD) s, respectively, which were significantly different ( $P < 0.05$  by Student's 2-tailed, paired *t*-test). Table 1 summarizes the supine and prone vertical gradients in MTT data using univariate linear regression for all eight animals. For all eight animals in the supine position, there was a positive linear relation between MTT and height for both lungs ( $P < 0.001$ ). The slopes

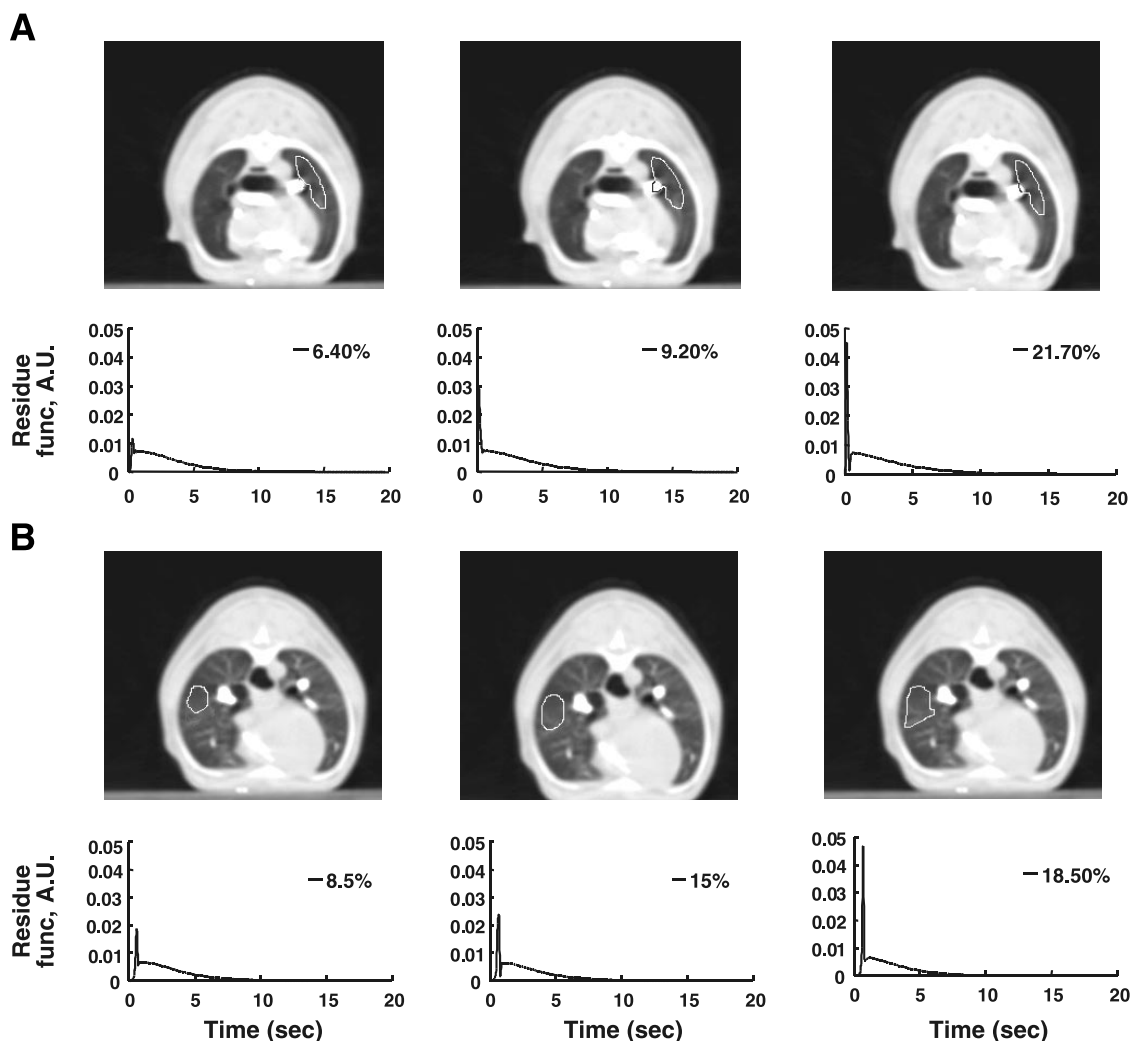


Fig. 5. Several ROIs containing increasing portions of pulmonary artery (A) along with lung parenchyma and several other parenchymal ROIs containing small peripheral arteries of increasing size (B). Because ROIs in A and B include a greater proportion of the pulmonary artery, the magnitude of the first sharp peak in the calculated residue functions (func) increases and the contamination index increases from 6.4 to 18.9% (A) and from 8.5 to 21.7% (B).

Table 1. *Supine and prone vertical gradients in MTTs*

Animal No.	Supine						Prone					
	Both lungs		Left lung		Right lung		Both lungs		Left lung		Right lung	
	Gradient	$R^2$	Gradient	$R^2$	Gradient	$R^2$	Gradient	$R^2$	Gradient	$R^2$	Gradient	$R^2$
1	0.27	0.16	0.30	0.18	0.26	0.15	-0.07	0.02	-0.13	0.05	-0.04	0.01
2	0.19	0.08	0.12	0.04	0.28	0.13	0.00	0.00	-0.09	0.02	0.05	0.01
3	0.46	0.28	0.44	0.28	0.49	0.29	0.05	0.00	0.03	0.00	0.08	0.01
4	0.21	0.19	0.20	0.20	0.23	0.18	-0.12	0.07	-0.15	0.10	-0.10	0.05
5	0.15	0.09	0.21	0.21	0.06	0.01	-0.05	0.00	-0.17	0.00	-0.07	0.09
6	0.14	0.14	0.16	0.17	0.13	0.11	-0.02	0.00	-0.01	0.00	-0.03	0.09
7	0.27	0.12	0.29	0.13	0.26	0.11	0.36*	0.13	0.33*	0.12	0.36*	0.12
8	0.28	0.11	0.25	0.08	0.31	0.15	0.27*	0.20	0.25*	0.19	0.29*	0.20
Mean	0.25	0.15	0.25	0.16	0.25	0.14	0.05 (-0.03)	0.05 (0.02)	0.01 (-0.09)	0.06 (0.03)	0.07 (-0.02)	0.05 (0.02)
±SD	±0.10	±0.07	±0.10	±0.08	±0.13	±0.08	±0.17 (±0.06)	±0.07 (±0.03)	±0.19 (±0.08)	±0.07 (±0.04)	±0.17 (±0.07)	±0.07 (±0.02)

Values are slopes of univariate regression, mean transit time (MTT) vs. height up the lung, with corresponding squared correlation coefficients ( $R^2$ ). Two animals showed unusually steep positive gradients in prone position indicated by \*. Means are listed with and without (in parentheses) these 2 outliers (see text).

were significantly greater than zero:  $P < 0.001$  by  $t$ -test and  $P < 0.01$  using Wilcoxon signed-rank test. The slope for the linear fit for six of the eight animals in the prone position was zero or negative, with two outliers showing positive slopes. Because of the strength of these outliers, we cannot say that the slopes for the animals in the prone position are significantly different from zero. Although these two animals behaved clearly differently from all others in this series, we were unable to identify a specific reason to eliminate them from the analysis. A comparison of the difference in slopes between the supine and prone positions for each animal (Table 1) showed strong support for the hypothesis that the slopes for animals in the supine position were greater than those for animals in the prone position:  $P < 0.01$  (paired  $t$ -test) and  $P < 0.02$  (Wilcoxon signed-rank test). We also describe the overall difference in MTT at extremes of height (Table 2). In the supine posture, there was a  $\sim 1.8$ -s difference in MTT compared with a  $< 0.5$ -s difference in the prone posture. This difference between prone and supine was statistically significant using the nonparametric Wilcoxon

signed-rank test and the paired  $t$ -test ( $P < 0.005$  for both tests). Figure 6 shows individual regression lines. Both methods of evaluation, with the exception of two outliers, demonstrate that, despite the reduction in the ventral-dorsal differences in microvascular MTT in the prone compared with the supine posture, the microvascular MTT remained smaller for the dorsal, basal lung region independent of body posture. Microvascular MTT slopes from the linear model and the microvascular MTT difference showed no right-to-left differences in the prone or supine postures ( $P > 0.7$  by Student's 2-tailed, paired  $t$ -test).

The distributions of the microvascular MTTs in the supine and prone positions are represented by a color-coded map in Fig. 7. The color index ranged from 0 s microvascular MTT (blue) to 8 s microvascular MTT (red). In the supine posture, red pixels are dominant in the nondependent lung region, whereas green pixels are dominant in dependent regions, indicating the strong vertical gradient from dependent to nondependent regions. However, in the prone position, the middle part of the color index bar is scattered throughout

Table 2. *Difference of MTTs in nondependent vs. dependent regions in supine and prone postures*

Animal No.	Supine			Prone		
	Both lungs	Left lung	Right lung	Both lungs	Left lung	Right lung
1	1.92	1.90	1.95	-0.56	-1.04	-0.35
2	0.92	0.66	1.20	-0.11	-0.85	0.13
3	2.72	2.79	2.64	-0.08	-0.41	0.24
4	1.71	1.72	1.66	-0.91	-1.18	-0.69
5	1.31	2.04	0.41	-1.01	-0.86	-1.11
6	1.57	1.65	1.50	-0.33	-0.33	-0.34
7	2.45	2.42	2.42	2.17*	2.28*	1.74*
8	1.65	1.18	2.38	1.52*	1.64*	1.41*
Mean	1.79	1.80	1.77	0.09 (-0.5)	-0.09 (-0.78)	0.13 (-0.35)
±SD	±0.58	±0.67	±0.74	±1.15 (±0.40)	±1.31 (±0.34)	±0.99 (±0.50)

Values are differences in MTT obtained from average MTT in upper 25% and lower 25% of lung. This gives a model-independent estimate of gradient. Two animals showed unusually steep positive gradients in prone position indicated by \*. Means are listed with and without (in parentheses) these 2 outliers (see text).

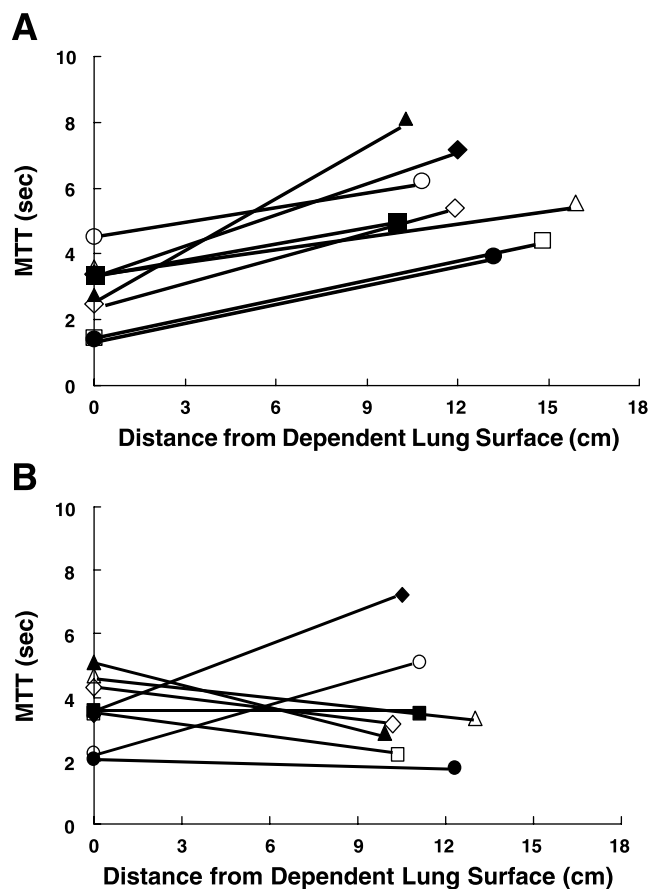


Fig. 6. Slopes of height vs. mean transit times (MTTs) using a linear regression model in supine (A) and prone (B) postures. Symbols do not represent data points; rather they are line labels. In the supine posture, 8 animals show positive slopes; in the prone posture, 5 animals display negative or zero slopes and 2 outliers show positive slopes. Slopes in the prone position are flatter than slopes in the supine position.

the whole lung, suggesting that there is minimal vertical gradient of microvascular MTT.

Figure 8 shows the distribution of air content (percent air) in the supine and prone postures. The color

index ranged from 0% air (blue) to 80% air (red). In the supine posture, the nondependent region is well expanded compared with the less expanded dependent lung region. This compares with the relatively uniform expansion seen in the prone position. This correlates well with previous CT observations (11) for which an earlier dynamic volumetric scanning method was used.

For the data obtained from five dogs, Monte Carlo simulation was performed to calculate the mean of the regional microvascular MTTs by addition of a globally or a locally calculated noise distribution (see APPENDIX) to fitted original data. Figure 9 shows a regression analysis of the original microvascular MTT against microvascular MTTs derived from data contaminated by local or global noise. The straight lines were fitted to the original microvascular MTT vs. microvascular MTT with local and global noise. The points on both graphs were contributed from the data of 5 dogs, where 10 samples (ROIs) were chosen from each dog. The slope of the original microvascular MTT and microvascular MTT with local noise is close to 1 ( $0.99 \pm 0.01$ ,  $R^2 = 0.99$ ). Similarly, the slope of the original microvascular MTT and microvascular MTT with global noise is close to 1 ( $0.96 \pm 0.09$ ,  $R^2 = 0.99$ ). The original mean microvascular MTT of  $4.27$  s vs. microvascular MTT with global noise of  $4.20 \pm 0.05$  (SE) s ( $P = 0.86$  by Student's 2-tailed, paired  $t$ -test) and the original microvascular MTT vs. microvascular MTT with local noise of  $4.23 \pm 0.01$  (SE) s ( $P = 0.79$ ) were not significantly different. These results demonstrate that measured imaging-derived noise does not have significant effects on the regional MTTs that are determined by application of our deconvolution-based algorithm. In addition, the means of standard errors of MTTs with global noise and local noise of 0.05 and 0.01, respectively, were small (Table 3).

## DISCUSSION

In this study, we refined our methods for calculating MTT in small lung regions using fast CT with rapid bolus injection of contrast agent. This technique allows

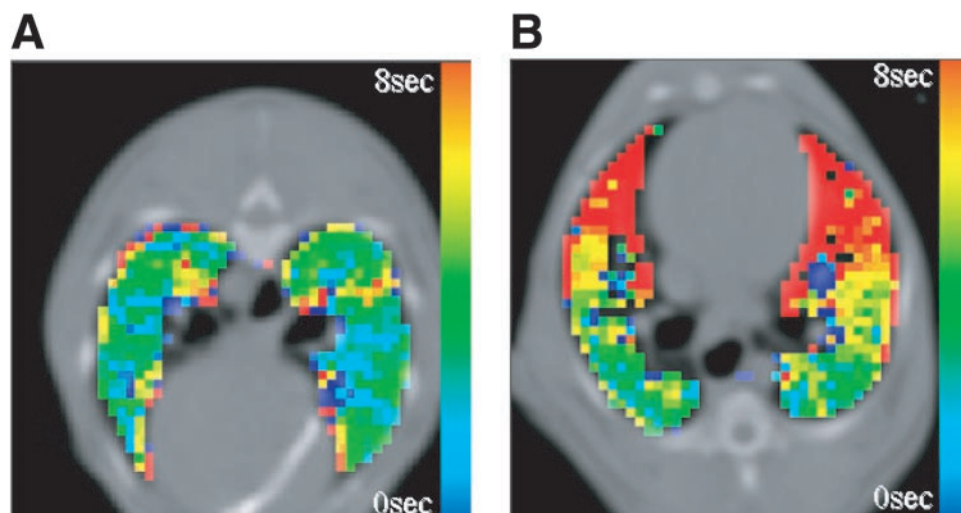
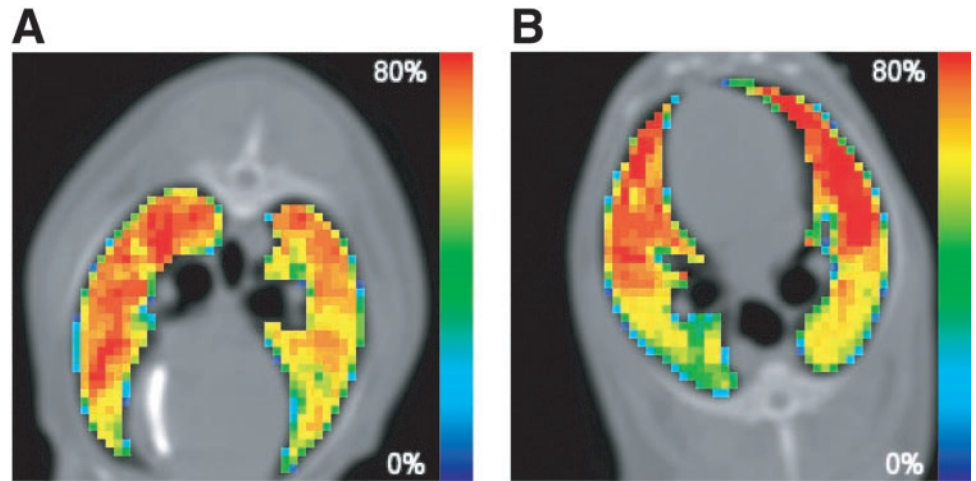


Fig. 7. Distribution of microvascular MTTs in prone (A) and supine (B) postures. Color index is shown at right: 0 s (blue) to 8 s (red). In supine posture, vertical gradient from dependent to nondependent regions is apparent; in prone posture, vertical gradient is so small that distribution of MTTs is indistinguishable from uniform.

Fig. 8. Distribution of air content (%air) in prone (A) and supine (B) postures. Color index is shown at right: 0% (blue) to 80% (red). Prone position shows a relatively more uniform expansion of the lung than supine posture. Trends in this physiological parameter correspond to previously reported pulmonary physiology.



separation of the true microvascular transport of the contrast agent from contaminating small arteries. We used a Monte Carlo technique to show a low susceptibility to noise, and we demonstrated gradients in microvascular MTTs that mostly agree with other studies.

The technique for determining regional MTTs and blood flow by following washin and washout of contrast agent has several theoretical shortcomings. 1) It is assumed that any given ROI contains only parenchyma and no feeding or draining vessels. The technique we present here allows us to detect the effects of larger arteries, but effects of small veins could still affect results. We try to minimize the effect of veins by fitting our gamma variate function only to the upper 50% of the downslope of the time-attenuation curve. 2) The regional residue function includes small precapillary arteries, capillaries, and small postcapillary veins. Thus the MTT data represent lumped effects of all three components of the microvessels above; thus, although our new method provides unique regional information in vivo, the results must be interpreted with the limitations in mind. 3) It is assumed that there is little washout of contrast agent from the veins at the time of the peak contrast concentration in the region.

This assumption is very difficult to test; however, in a study of the passage of labeled RBCs through isolated lungs, Beck (3) found that a correction for venous washout had a very small effect on results. However, the assumption remains largely untested in vivo.

Validation of any method for determining MTT is difficult, because there is no accepted "gold standard" against which to compare a new method. Previous attempts to measure MTTs have included methods to obtain global average MTTs from the ratio of blood volume to total flow and relatively invasive and destructive methods that access only surface vessels. Thus our approach to validation for this study was to show that results were in reasonable agreement with previous studies and that regional gradients in MTT are consistent with known vascular physiology.

In a previous preliminary study, we showed that the deconvolved residue function has a bimodal characteristic that consists of the first sharp, narrow peak, which we believed represented the partial volume averaging of small arteries, and the second smooth, broad curve, which indicated the pure microvascular portion of the residue function (28). Supporting this notion are the data obtained through deconvolving time-attenuation curves taken from visually apparent small arteries

Fig. 9. Slopes and correlations of MTT of original data vs. MTT with local noise (A) and MTT of original data vs. MTT with global noise (B). Data from 5 dogs were used for Monte Carlo simulations. Both slopes are insignificantly different from 1. Original MTT and MTT with local or global noise were highly correlated. Addition of local noise leads to a better result than addition of global noise. This is expected, because standard deviation in noise distribution is larger for global than for local noise.

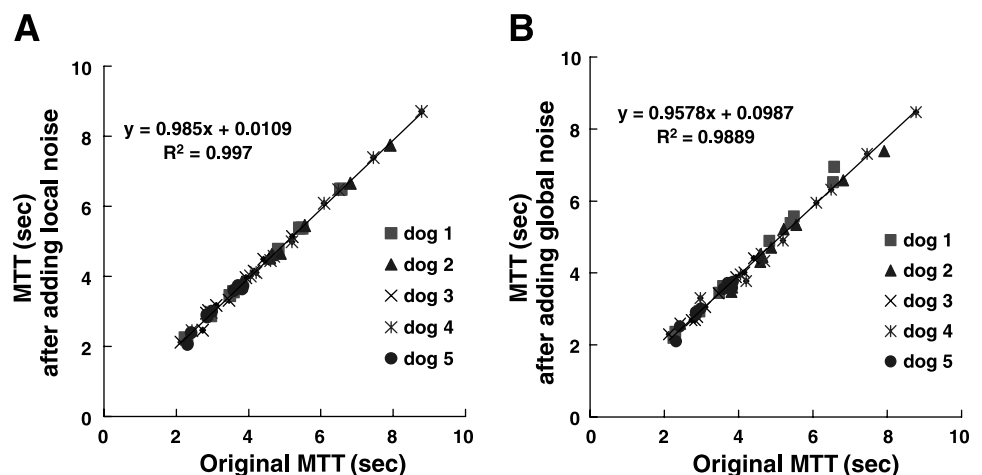


Table 3. Monte Carlo simulation of MTT

Dog No.	Original	Global Noise		Local Noise	
	MTT	MTT	SE	MTT	SE
1	4.34	4.39	0.04	4.29	0.01
2	5.18	4.96	0.07	5.09	0.02
3	3.21	3.19	0.03	3.21	0.01
4	5.45	5.28	0.06	5.38	0.02
5	3.21	3.17	0.03	3.16	0.01
Mean	4.28	4.20	0.05	4.23	0.01

Data were obtained by applying curve-fitting algorithms to raw data obtained by using original data, global noise, and local noise for 5 dogs.

in the lung field. The deconvolved residue functions from these samples are composed almost exclusively of a sharp, narrow peak. The data (Fig. 4) showing a reduction in the arterial peak as ROI locations were moved from dependent to nondependent lung regions can be explained as follows. 1) Because of the greater number of arterial vessels per ROI in the dependent (dorsal) lung regions of the canine pulmonary vascular architecture of the dog, there are a greater number of arterial vessels per ROI in the dependent (dorsal) lung regions. 2) Because of a vertical gradient in regional lung expansion in the supine posture, the lungs are more compressed (less expanded) in the dependent regions (Fig. 8), thus resulting in a greater numbers of partial volumed small arteries per ROI in the dependent lung. 3) Flow is lower in the nondependent regions of the supine dog. In this study, the samples that included different proportions of a visibly identifiable artery along with parenchymal regions of lung were selected. Regardless of the region of the lung, the greater the visible arterial component, the larger were the contamination indexes calculated by Eq. 6. These data support the notion that the first sharp peak of the residue function represents partial-volume small arteries, in addition to microvasculature, that are not visibly apparent in the lung parenchymal ROIs. Data are consistent with known pulmonary anatomy and physiology.

Deconvolution using the FFT method is known to be sensitive to noise (1). In the present study, we introduced and applied the DLS approach to investigate whether the first sharp, narrow peak in the residue function could be generated by noise effects on the FFT method. Clough et al. (7) used the DLS method to obtain organ transport functions through deconvolution of input and output concentration curves. We utilized the DLS algorithm, because this algorithm can reduce or remove the noise generated during deconvolution by using a regularization method introduced by Tikhonov and Arsenin (30). Fitted curves of the residue function obtained by using the deconvolution method and the DLS method closely matched each other and showed bimodal characteristics. After the resultant functions from the two methods were reconvolved with the input curves, the original output curves also matched closely the two reconvolved curves. By using

the FFT deconvolution method, some of the first sharp peaks of the residue function were affected by noise, and their magnitude tended to increase. However, the second broad curve of each residue function remained intact under the influence of noise. The microvascular MTTs that are calculated using only the second broad curve of the residue function after removal of the first peak remained similar between the two methods of deconvolution. The Monte Carlo approach allows the exploration of various analytic approaches that may be difficult or laborious to implement experimentally (9, 23). We used the Monte Carlo technique to estimate the error in our deconvolution-based regional microvascular MTT measures. Noise chosen locally and globally from a series of images was superimposed on the original data to create fluctuations in the simulated density measurement. There are multiple real sources for the variability of noise. Motion of the lung results in changes in the exact tissue elements imaged in each ROI. Small changes in the amount of denser tissue elements, such as vessels, airway wall, and connective tissue, change the average ROI density according to their fractional volume. Thus the effects of lung motion increase as ROI and slice thickness decrease. Our study indicates that the mean microvascular MTT calculated from the original data was 4.28 s compared with microvascular MTT with global noise,  $4.20 \pm 0.05$  (SE) s, and microvascular MTT with local noise,  $4.23 \pm 0.01$  (SE) s, showing that original MTT and MTT simulated with noise were not significantly different ( $P > 0.8$ ). Also, regression analysis using original MTT vs. local noise MTT and original MTT vs. global noise MTT demonstrated that the slopes were 0.99 and 0.96, respectively. When several factors, such as the number of parameters used in a gamma variate curve for fitting, the degree of noise, and FFT deconvolution, are considered, the above results demonstrate the robust nature of our algorithm (including the selected FFT deconvolution method) to obtain microvascular MTTs.

The anatomic distributions of pulmonary capillary (plasma) and RBC MTTs have been measured by other investigators (5, 15). Presson et al. (21) showed, using in vivo microscopy, that RBC MTT was 1.4 times faster than plasma MTT, because RBCs travel down the center of the vessels where velocity is greatest. Both transit times depend on the cardiac output, blood volume, and capillary recruitment. For example, the higher the cardiac output, the faster are pulmonary capillary and RBC MTTs (5). According to in vivo microscopy results of Wagner et al. (32), capillary MTTs were  $12.3 \pm 2.5$  s in the nondependent lung,  $3.1 \pm 0.6$  s in the middle lung, and  $1.6 \pm 2.5$  s in the dependent lung when the dogs were placed in the lateral decubitus position. In our study, microvascular MTTs in the supine and prone postures were  $3.94 \pm 1.03$  and  $3.4 \pm 0.86$  (SD) s, respectively. Even though exact experimental equivalence is difficult to judge between our studies and the in vivo microscopy studies because of such factors as the different methods of measurement, possible differences in cardiac output, and different body postures, it appears that both MTTs

are within similar magnitudes. Other investigators, including the *in vivo* microscopy group of Wagner et al. (32), showed the existence of a vertical gradient of pulmonary capillary (plasma) and RBC MTTs using different animal and body positions with the exception of the prone posture (10, 17, 18, 32). Their studies demonstrated a clear gravitationally oriented difference within the lungs, with the shortest transit times in the most dependent regions.

In our study, we applied linear and nonlinear models to determine the dependent-to-nondependent differences in MTT in the supine and prone body postures. Both models showed that the dorsal-to-ventral gradient in MTT in the supine posture is significantly reduced in the prone posture in most of our animals. Vertical gradients of capillary transit times have been investigated by others (10, 32) using imaging- and non-imaging based-methods. Wagner et al. (32) measured the capillary transit times in the upper (zone 2), middle (between zone 2 and 3), and lower (zone 3) regions of the lung of dogs and demonstrated that the transit times decreased progressively from nondependent lung to dependent lung. Therefore, they concluded that the most recruitable capillary beds and fastest transit times are in the gravitationally dependent lung. Also, human studies showed that RBC transit times are shorter in the dependent region of the lung in humans studied in the lateral decubitus position.

In summary, the FFT-based deconvolution used in this study is computationally efficient and speedy. The FFT-based algorithm we have implemented is also model free, so that the residue function is not constrained to any predefined shape or form. It is unlikely that we would have been successful had we used other deconvolution techniques that assume a shape for the residue function. Supporting the validity of the EBCT-derived regional MTT measurements is the close agreement between capillary MTTs calculated from the recovered microvascular components and direct microvascular observations reported by others, as well as the small error between original data MTTs and MTTs obtained by Monte Carlo simulation. Also the vertical gradient between dependent and nondependent regions is smaller in the prone than in the supine posture. The close agreement between the EBCT-derived data and the direct observations (*in vivo* microscopy) of others suggests that dynamic X-ray CT imaging in conjunction with a deconvolution-based algorithm offers a unique method to noninvasively quantitate *in vivo* regional microvascular perfusion, volumes, and transit times throughout the lungs. More recently, subsecond multiple detector-row spiral (helical) CT scanners have been introduced with scan times approaching the times required for quantitative pulmonary function evaluation (24). The present work will readily translate to this newly emerging, more widespread technology.

## APPENDIX

*Monte Carlo simulations.* To estimate the error in our deconvolution-based regional microvascular MTT measures,

random errors were superimposed on known input (pulmonary artery) and output (regional parenchymal) time-attenuation curves. The resulting simulated data were then fit to gamma variate functions and processed via deconvolution algorithms to provide microvascular MTT measures for the simulated curves.

Images of a physical airway tree cast were obtained via EBCT and used to measure the noise. This physical airway phantom was a hollow rubber cast of a postmortem human lung. The cast was placed in a Plexiglas cylinder filled with dried potato flakes to represent the lung tissue. Images were obtained at 8 levels and 20 time points per level. The noise present in the "dynamic" images was measured globally and locally. Each noise measurement was used for the simulation separately.

The "global noise" was obtained by using the following steps. 1) The attenuation value (Hounsfield unit) of each pixel across 20 time points was summed and averaged using Eq. 7, because the averaged image can be considered a noise-free image. 2) The averaged image was subtracted from each of the original images by Eq. 8, which can be considered the image that contains only noise. Application of the Kolmogorov-Smirnov test for normality showed that the global noise obtained was normally distributed with a mean of  $-0.43$  and a standard deviation of  $3.93$ . Therefore, the global noise was modeled as a normally distributed variable with zero mean and a variance of  $3.93$

$$\text{Avg}_{\text{image}}(x, y) = \sum_{t=1}^N I(x, y) / N, N = 20 \quad (7)$$

$$\text{Dif}_{\text{image}}(x, y) = \text{Avg}_{\text{image}}(x, y) - I(x, y) \quad (8)$$

where  $\text{Avg}_{\text{image}}$  is the average (noise-free) image,  $I(x, y)$  is the pixel value of the original image, and  $\text{Dif}_{\text{image}}(x, y)$  is the difference between original image and  $\text{Avg}_{\text{image}}(x, y)$  at location coordinates  $(x, y)$ .

The "local noise" was measured by subtracting the mean of a  $5 \times 5$  pixel (ROI) sample from the mean of a  $5 \times 5$  pixel sample on the next image with the process repeated through the consecutively acquired images of the airway tree phantom as follows

$$\text{Mean}_t(x, y) = \sum_{i=-2}^2 \sum_{j=-2}^2 I_t(x+i, y+j) / 5 \quad (9)$$

$$\text{Mean}_{t+1}(x, y) = \sum_{i=-2}^2 \sum_{j=-2}^2 I_{t+1}(x+i, y+j) / 5 \quad (10)$$

$$\text{Dif}_t(x, y) = \text{mean}_t(x, y) - \text{mean}_{t+1}(x, y), \quad t = 1, \dots, 10 \quad (11)$$

where  $\text{mean}_t(x, y)$  is the mean pixel value of a  $5 \times 5$  region in the  $t$ th image,  $I_t(x, y)$  at position coordinates  $(x, y)$ .  $\text{Dif}_t(x, y)$  is the difference between the mean value calculated between two images.

The global noise with normal distribution (zero mean and standard deviation of  $3.93$ ) and the local noise obtained by the local difference value of mean were applied separately for the Monte Carlo simulation. Each simulation followed the same steps: 1) The feeding and regional parenchymal time-attenuation curves were chosen from dog images and fitted by a gamma variate function. 2) Global or local noise was added to the corresponding attenuation values at each time point of the fitted pulmonary artery and parenchymal time-attenuation curves obtained above. 3) The resulting simu-

lated data were fit to a gamma variate function, sampled with a temporal resolution of 0.05 s, and deconvolved via the FFT-based algorithm. The putative microvascular component of the resulting residue function was isolated, and a MTT for the microvascular bed was calculated as the ratio of peak to area of the microvascular component of the residue function.

A total of 100 simulations were performed for each of 10 samples from 5 dog data sets.

The authors thank Osama Saba.

This study was supported in part by National Heart, Lung, and Blood Institute Bioengineering Research Partnership RO1 HL-64368.

## REFERENCES

1. **Axel L.** Tissue mean transit time from dynamic computed tomography by a simple deconvolution technique. *Invest Radiol* 18: 94–99, 1983.
2. **Bassingthwaite JB, Raymond GR, and Chan JIS.** *Nuclear Cardiology: State of the Art and Future Directions*, edited by Beller GA. St. Louis, MO: Mosby-Year Book, 1993, p. 3–23.
3. **Beck KC.** Regional trapping of microspheres in the lung compares well with regional blood flow. *J Appl Physiol* 63: 883–889, 1987.
4. **Boyd DP and Lipton MJ.** Cardiac computed tomography. *Proc IEEE* 71: 298–307, 1983.
5. **Capen RL, Hanson WL, Latham LP, Dawson CA, and Wagner WWJ.** Distribution of pulmonary capillary transit times in recruited networks. *J Appl Physiol* 69: 473–478, 1990.
6. **Capen RL, Latham LP, and Wagner WWJ.** Comparison of direct and indirect measurements of pulmonary capillary transit times. *J Appl Physiol* 62: 1150–1154, 1987.
7. **Clough AV, Cui D, Linehan JH, Krenz GS, Dawson CA, and Maron MB.** Model-free numerical deconvolution of recirculating indicator concentration curves. *J Appl Physiol* 74: 1444–1453, 1993.
8. **Davenport R.** The derivation of the gamma-variate relationship for tracer-dilution curves. *J Nucl Med* 24: 945–948, 1983.
9. **Hanger CC, Presson RGJ, Okada O, Janke SJ, Watkins JJ, and Wagner WWJ.** Computer determination of perfusion patterns in pulmonary capillary networks. *J Appl Physiol* 82: 1283–1289, 1997.
10. **Hatabu H, Tadaura E, Levin DL, Chen Q, Li W, Kim D, Prasad PV, and Edelman RR.** Quantitative assessment of pulmonary perfusion with dynamic contrast-enhanced MRI. *Magn Reson Med* 42: 1033–1038, 1999.
11. **Hoffman EA.** Effect of body orientation on regional lung expansion: a computed tomographic approach. *J Appl Physiol* 54: 468–480, 1985.
12. **Hoffman EA, Acharya RS, and Wollins JA.** Computer-aided analysis of regional lung air content using three-dimensional computed tomographic images and multinomial models. *Int J Math Modeling* 7: 1099–1116, 1986.
13. **Hoffman EA and Tajik JK.** Dynamic and high-resolution CT assessment of pulmonary blood flow distribution (Abstract). *Am Rev Respir Dis* 147: A1201, 1993.
14. **Hoffman EA, Tajik JK, and Kugelmass SD.** Matching pulmonary structure and perfusion via combined dynamic multi-slice CT and thin-slice high-resolution CT. *Comput Med Imaging Graph* 19: 101–112, 1995.
15. **Hogg JC, Martin A, Lee S, and McLean T.** Regional differences in erythrocyte transit in normal lungs. *J Appl Physiol* 59: 1266–1271, 1985.
16. **Jones AT, Hansell DM, and Evans TW.** Pulmonary perfusion in supine and prone position: an electron-beam computed tomography study. *J Appl Physiol* 90: 1342–1348, 2001.
17. **Levin DL, Chen Q, Zhang M, Edelman RR, and Hatabu H.** Evaluation of regional pulmonary perfusion using ultrafast magnetic resonance imaging. *Magn Reson Med* 46: 166–171, 2001.
18. **Macnee W, Martin BA, Wiggs BR, Belzberg AS, and Hogg JC.** Regional pulmonary transit time in humans. *J Appl Physiol* 66: 844–850, 1989.
19. **Marcucci C, Nyhan D, and Simon BA.** Distribution of pulmonary ventilation using Xe-enhanced computed tomography in prone and supine dogs. *J Appl Physiol* 90: 421–430, 2001.
20. **Ostergaard L, Weisskoff RM, Chesler DA, Gyldensted C, and Rosen BR.** High-resolution measurement of cerebral blood flow using intravascular tracer bolus passages. 1. Mathematical approach and statistical analysis. *Magn Reson Med* 36: 715–725, 1996.
21. **Presson RG, Graham JA, Hanger CC, Godbey PS, Gebb SA, Sidner RA, Glenny RW, and Wagner WW.** Distribution of pulmonary capillary red blood cell transit times. *J Appl Physiol* 79: 382–388, 1995.
22. **Rempp KA, Brix G, Wenz F, Becker CR, Guckel F, and Lorenz WJ.** Quantification of regional cerebral blood flow and volume with dynamic susceptibility contrast-enhanced MR imaging. *Radiology* 193: 637–641, 1994.
23. **Simon BA, Marcucci C, Fung M, and Lele SR.** Parameter estimation and confidence intervals for Xe-CT ventilation studies: a Monte Carlo approach. *J Appl Physiol* 84: 709–716, 1998.
24. **Tajik JK, Chon D, Won C, Tran BQ, and Hoffman EA.** Subsecond multisection CT of regional pulmonary ventilation. *Acad Radiol* 9: 130–146, 2002.
25. **Tajik JK, Kugelmass SD, and Hoffman EA.** An automated method for relating regional pulmonary structure and function: integration of dynamic multislice CT and thin-slice high-resolution CT. *Proc SPIE Med Imaging* 1905: 339–350, 1993.
26. **Tajik JK, Tran BQ, and Hoffman EA.** Assessing regional pulmonary microvascular transit times and flows using dynamic multislice CT (Abstract). *Am J Respir Crit Care Med* 153: A816, 1996.
27. **Tajik JK, Tran BQ, and Hoffman EA.** Xenon-enhanced CT imaging of local pulmonary ventilation. *Proc SPIE Med Imaging* 2709: 40–54, 1996.
28. **Tajik JK, Tran BQ, and Hoffman EA.** New technique to quantitate regional pulmonary microvascular transit times from dynamic X-ray CT images. *SPIE Med Imaging Physiol Function Multidimensional Images* 3337: 24–32, 1998.
29. **Thompson HK, Starmer F, Whalen RE, and McIntosh HD.** Indicator transit time considered as a gamma variate. *Circ Res* 14: 502–515, 1964.
30. **Tikhonov A and Arsenin V.** *Solutions of Ill-Posed Problems*. London: Wiley/Winston, 1977.
31. **Wagner WWJ, Latham LP, Gillespie MN, Guenther P, and Capen RL.** Direct measurement of pulmonary capillary transit times. *Science* 218: 379–381, 1982.
32. **Wagner WWJ, Latham LP, Hanson WL, Hofmeister SE, and Capen RL.** Vertical gradient of pulmonary capillary transit time. *J Appl Physiol* 61: 1270–1274, 1986.